Large Eddy Simulation of Axisymmetric Scramjet Based on Dynamic Zone Flamelet Model

Wenming Sun, Hang Liu, Long Li, and Wei Yao

Abstract To verify the effectiveness of a novel axisymmetric scramjet, Improved Delay Detached Eddy Simulation (IDDES) coupled with Dynamic Zone Flamelet Model (DZFM) based on 60 million cells was conducted to investigate the performance of the full-scale engine. Four mesh sets with different refinement levels and adopting hexahedral structured cells were used for the grid independence verification. The pressure agrees well with the experimental data. Due to the absence of the corner effect, the boundary layer is thinner and the jet penetration depth is low. The poor mixing between the transverse fuel jet and the crossflow causes weak combustion and a low-pressure rise ratio. The cavity plays four roles in enhancing combustion: a radial pool, a low-speed bay, a high-temperature zone, and a premixer. Axisymmetric scramjets without any flame holders overall have poor mixing and combustion performance.

Keywords Axisymmetric scramjet · Ethylene · Improved Delay Detached Eddy Simulation (IDDES) · Dynamic Zone Flamelet Model (DZFM) · Cavity

1 Introduction

Scramjet does not need to carry the oxidizer and has excellent endurance performance. Since the proposal of its concept, it has been persistently studied for nearly 60 years [1–7]. The fuel of scramjet can be typically classified as hydrogen fuel and hydrocarbon fuel. With higher energy density and lower ignition delay, hydrogen fuel has a higher upper limit of flight speed and altitude and generally does not need any flame ignition devices. While the ignition delay of hydrocarbon fuel is in the order of milliseconds, which is close to the residence time in the scramjet. This will bring great challenges to the starting, operation, and endurance of the scramjet. Researchers

W. Sun · L. Li · W. Yao (✉)
Institute of Mechanics, CAS, Key Laboratory of High-Temperature Gas Dynamics, Beijing, China
e-mail: weiyao@imech.ac.cn

H. Liu · W. Yao
School of Engineering Science, University of Chinese Academy of Science, Beijing, China

S. Lee et al. (eds.), *The Proceedings of the 2021 Asia-Pacific International Symposium on Aerospace Technology (APISAT 2021), Volume 2*, Lecture Notes in Electrical Engineering 913, https://doi.org/10.1007/978-981-19-2635-8_90

have tried various configurations to achieve good ignition, flame stabilization, and high combustion efficiency for hydrocarbon-fueled scramjet. In fact, hydrogen fuel is often used as the ignition source before the injection of hydrocarbon [8].

The earliest scramjet was used in missile systems [9]. The combustors and compressors used by JHU/APL in the early 1960s were both circular. There are three main advantages of adopting a circular inlet and combustor during this period. The primary advantage is because of the lighter weight of the circular structure. Under the same hoop pressure, the axisymmetric structure will not produce bending stress, which can cause fatigue cracks. The rectangular structure must be relieved by using a relatively heavy back structure. The vehicle weight will have a direct impact on the continuation of the journey. When the weight increases by 8%, the endurance range will even be reduced to 65% of the rated mileage [10]. Therefore, the circular structure is extremely beneficial, especially in the early stage. The second advantage is reducing the need for cooling and internal resistance. When the flow area is fixed, the wetted area generated by the circular cross-section is the smallest, so the surface cooling and friction resistance will be reduced accordingly. The last advantage is reducing the length of the engine body. The axisymmetric compressor belongs to the three-dimensional geometry, which has better compression performance than the two-dimensional one. Therefore, the length of the engine fuselage can be shortened, which further reduces the vehicle weight and enhances the endurance capability.

However, in the 1980s, NASP abandoned the axisymmetric structure and adopted a rectangular structure. There are at least four reasons for this decision. 1) Due to the need to obtain long endurance, the vehicle needs to fly in a predetermined flight envelope. However, the NASP Single Stage-To-Orbit (SSTO) flight plan covers a very wide flight envelope (from the lower limit of the ramjet to the scramjet cruising), which makes the flight speed range across at least 3 Mach numbers. The extremely wide speed range makes the best response plan to be an adjustable compressor. The two-dimensional compressor has a more convenient adjustment method relative to the axisymmetric one. 2) The second reason is to achieve excellent fuel mixing performance. The rectangular combustor can have a shorter gap compared to the axisymmetric combustor and has excellent mixing performance when the penetration depth is relatively small. The mixing process directly determines the combustion performance and further affects the cruising range. 3) For the Rocket-Based Combined Cycle (RBCC) system, the compressor of the ramjet is generally set as a spatula type to better combine the two engine parts to maintain a higher lift-to-drag ratio. This structure has been inherited since the adoption of NASA ISTAR. 4) The flow field of the inlet of the parallel RBCC structure is very complicated, which requires very powerful calculation capabilities. The two-dimensional inlet is relatively simple, which brings greater convenience to the modeling and the analysis of combustion performance.

In recent years, the development of scramjets makes them the most potential candidate for hypersonic cruise vehicles, and the demand for speed range has been reduced. The development of Computational Fluid Dynamics (CFD) technology makes fast and complex modeling be reality. The change in fuel injection mode further compensates for the shortcomings of the circular combustor. Therefore, the

circular combustor design re-attracts research interest and will become one of the main trends in the future. This study presents the LES modeling of an axisymmetric scramjet combustor with a novel zone-based combustion model to reveal the flow and combustion characteristics, to provide design guidance for future axisymmetric scramjets.

2 Model and Case

2.1 Experimental Case

The axisymmetric scramjet modeled in this study is based on the experimental study of Vanyai et al. [11]. With a full length of 661.4 mm, the model is composed of three parts, i.e., compressor, isolator, and combustor. Detailed geometric configurations of the scramjet and the cavity are shown in Fig. 1. The total length of the compressor is 211.4 mm, which can be divided into two parts. The upstream part connects directly with the incoming flow, with a total length of 33.2 mm and a contraction angle of 1.85°. The downstream part connects to the isolation section and it has a curved configuration to suppress the shock waves. The compressor can reduce the incoming flow from Mach 4 to Mach 3. The length of the straight isolator is 20 0 mm. To increase the jet penetration depth, the fuel is injected into the isolator section because of its smaller radius. Moreover, the upstream fuel injection increases the fuel mixing distance. Ethylene is injected at sonic speed from 8 evenly distributed portholes, each with a diameter of 0.1 mm. The center of the porthole is 20 mm in front of the cavity leading edge. The fuel injection angle is 45° relative to the isolator wall. To stabilize the flame, the combustor adopts a classic cavity [12–14] whose depth is 8 mm, the aft angle of the trailing edge is 22.5°, and the full length is 41.7 mm. The designed flight Mach number is 7–8, and the flight dynamic pressure is 100 kPa. The mass flow rate of the ethylene fuel is 23.552 g/s, which corresponds to an equivalent ratio of 0.29. The detailed incoming flow parameters are summarized in Table 1.

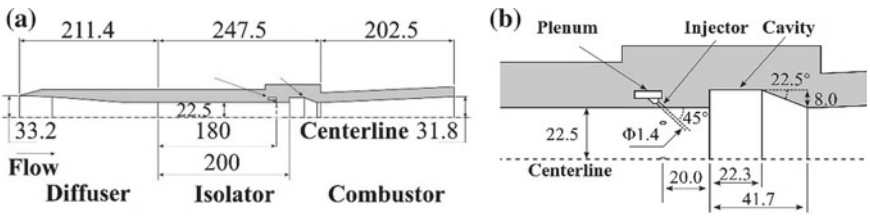

Fig. 1 **a** Geometry and **b** cavity of the axisymmetric scramjet

Table 1 Flow conditions of the freestream

Freestream (mass fraction Y_{N2}: 0.767, Y_{O2}: 0.233)	
Stagnation temperature (K)	2550
Stagnation pressure (kPa)	4500
Mach number	3.87
Static temperature (K)	669.6
Static pressure (kPa)	33.4
Density (kg/m^3)	0.173
Velocity (m/s)	1994

2.2 *Flow Solver: Amber*

The modeling is based on the compressible reaction flow solver Amber, which is developed from the standard compressible flow solver rhoCentralFoam [15]. The main improvement is adding a full-species transportation module with multi-component diffusion and turbulent combustion module. The coupling with the chemistry solving package CHEMKIN II [16] enables the accurate calculation of multi-component thermophysical and transport properties. Using a semi-discrete central Kurganov-Noelle-Petrova (KNP) scheme [17, 18], the second accuracy of nonlinear inviscid convective fluxes is achieved. The KNP scheme inherited from rhoCenter-Foam exhibits good performance in resolving discontinuities and high efficiency for its Riemann-free simplicity. The time integration is based on the second-order Crank–Nicolson scheme. The volume integration of the spatial gradient, divergence, and Laplacian terms in the partial differential equations (PDEs) are discretized as the Gauss face integration and the face values are interpolated by the third-order scale-selective discretization (SSD) scheme [19]. The thermodynamic and transport properties of individual species are calculated based on the NIST-JANAF thermophysical and transport database [20].

Amber has been extensively validated for various frozen flows, including the canonical shock tube problem, forward step flow, hypersonic flow over a biconic, and supersonic jets [21–27]. Various scramjet combustor cases [28–33] used this solver to examine its accuracy and robustness in the modeling of complex supersonic combustions.

2.3 *Governing Equations*

The filtered Favre-averaged conservation equations of mass, momentum, energy and species concentration used are defined as,

$$\frac{\partial \overline{\rho}}{\partial t} + \frac{\partial \overline{\rho} \tilde{u}_i}{\partial x_i} = 0 \tag{1}$$

$$\frac{\partial \overline{\rho}\tilde{u}_i}{\partial t} + \frac{\partial \overline{\rho}\tilde{u}_i\tilde{u}_j}{\partial x_j} = -\frac{\partial \overline{p}}{\partial x_i} + \frac{\partial \widetilde{\tau}_{ij}}{\partial x_j} - \frac{\partial \tau_{ij}^{sgs}}{\partial x_j} + \frac{\partial D_{ij}^{sgs}}{\partial x_j} \tag{2}$$

$$\frac{\partial \overline{\rho}\widetilde{\mathrm{H_t}}}{\partial \mathrm{t}} + \frac{\partial \overline{\rho}\widetilde{\mathrm{u}}_\mathrm{j}\widetilde{\mathrm{H_t}}}{\partial \mathrm{x_j}} - \frac{\partial}{\partial \mathrm{x_j}}\left(\overline{\rho}\mathrm{D_T}\frac{\partial \widetilde{\mathrm{H_t}}}{\partial \mathrm{x_j}} + \sum_{\alpha=1}^{\mathrm{L}}\overline{\rho}\mathrm{D}_\alpha\frac{\partial \widetilde{\mathrm{Y}}_\alpha}{\partial \mathrm{x_j}}\widetilde{\mathrm{H}}_\alpha\right) - \frac{\partial \overline{\mathrm{p}}}{\partial \mathrm{t}} - \frac{\partial \widetilde{\mathrm{u}}_\mathrm{j}\,\widetilde{\tau}_{\mathrm{ij}}}{\partial \mathrm{x_j}} = -\frac{\partial H_i^{sgs}}{\partial \mathrm{x_j}} + \frac{\partial \sigma_i^{sgs}}{\partial x_i} \tag{3}$$

$$\rho_\eta\frac{\partial \mathrm{Q}_\alpha}{\partial \mathrm{t}} + \langle \rho \mathrm{u_j}|\eta\rangle_{\mathrm{zone}}\frac{\partial \mathrm{Q}_\alpha}{\partial \mathrm{x_j}} = \rho_\eta\frac{\mathrm{D}_\alpha}{\mathrm{D}_\xi}\langle\chi|\eta\rangle_{\mathrm{zone}}\frac{\partial^2 \mathrm{Q}_\alpha}{\partial \eta^2} + \rho_\eta\langle \mathrm{W}_\alpha|\eta\rangle \tag{4}$$

$$\overline{p} = \overline{\rho}R\tilde{T} + R_u\sum_{k=1}^{N}T^{sgs} \tag{5}$$

where the overbar (" − ") and tilde ("∼") mean the cell and Favre average, respectively; ρ is the density; u_i is the velocity in the $\mathrm{x_i}$ direction; p is the pressure; τ_{ij} is the viscous stress tensor; h_s is the sensible enthalpy per unit mass; q_i is the heat flux vector; Y_α is the species mass fraction; D_ξ and D_α means the diffusivities of the mixture parcels and individual species respectively; $\tilde{T}$ is the temperature; R is the gas constant of gas mixture; R_u is the universal gas constant; W_α is the reaction rate with units s^{-1}. Note that extended flamelet equations Eq. (4) is solved instead of the traditional mean species equation. The mean species mass fractions $\widetilde{Y}_\alpha$ are then recovered by PDF weighted integration of Q_α over the mixture fraction space.

There are "sgs" superscripts in Eq. (1–5), which lead to the unclose of these equations, SGS is the shortcut of Subgrid-Scale. D_{ij}^{sgs} is SGS viscous stress, σ_i^{sgs} is SGS viscous diffusion, $\theta_{k,j}^{sgs}$ is SGS species diffusive fluxes, T^{sgs} is SGS species-temperature correlation. And they are defined as $D_{ij}^{sgs} = \overline{\tau}_{ij} - \widetilde{\tau}_{ij}$, $\sigma_i^{sgs} = \mu_j\widetilde{\tau}_{ij} - \widetilde{\mu}_j\widetilde{\tau}_{ij}$, $T^{sgs} = \overline{\rho}(\widetilde{Y_kT} - \tilde{Y}_k\tilde{T})$, all of these factors are assumed to be small and neglected in this study [34–37]. The contribution of T^{sgs} is also neglected in the equation of state. H_i^{sgs} is SGS energy flux and can be defined as $H_i^{sgs} = \left(\overline{\rho}\,\widetilde{H_tu_i} - \overline{\rho}\,\widetilde{H_t}\widetilde{u_i}\right) + (\overline{pu_i} - \overline{p}\tilde{u}_i)$, which is modeled based on a linear eddy diffusivity assumption as

$$H_j^{sgs} = -\overline{\rho}\frac{\upsilon_{sgs}}{Pr_t}\frac{\partial \widetilde{\mathrm{H_t}}}{\partial x_j} = -\overline{\rho}\frac{\upsilon_{sgs}}{Pr_t}\left(\frac{\partial \tilde{H}}{\partial x_j} + \tilde{u}_i\frac{\partial \tilde{u}_i}{\partial x_j} + \frac{\partial k^{sgs}}{\partial x_j}\right) \tag{6}$$

where υ_{sgs} is eddy viscosity. τ_{ij}^{sgs} is SGS stress and can be defined as $\tau_{ij}^{sgs} = \overline{\rho}(\widetilde{u_iu_j} - \tilde{u}_i\,\widetilde{u_j})$, sub-grid stress model can extract energy from the resolved scales and model the drain associated with the energy cascade. τ_{ij}^{sgs} can be simulated by the eddy-viscosity model,

$$\tau_{ij}^{sgs} - \frac{2\delta_{ij}}{3}\overline{\rho}k^{sgs} = -2\nu_t\overline{\rho}[\tilde{S}_{ij} - \frac{\delta_{ij}}{3}\tilde{S}_{kk}] \tag{7}$$

where k^{sgs} is the SGS turbulent kinetic energy, $\tilde{S}_{ij}$ is the strain rate tensor for the resolved scale and can be defined as,

$$\tilde{S}_{ij} = \frac{1}{2}(\frac{\partial\tilde{u}_i}{\partial x_j} + \frac{\partial\tilde{u}_j}{\partial x_i}) \tag{8}$$

In this study, the turbulence viscosity is given by Improved Delayed Detached Eddy Simulation (IDDES) [38] based on the background RANS model one-equation Spalart–Allmaras model [39], to alleviate the computational cost in the boundary layer modeling while retaining LES accuracy in the internal flow.

2.4 Combustion Modeling

As a complex space–time multi-scale problem, supersonic combustion involves turbulence-chemistry interaction (TCI), which brings difficulties to high-fidelity modelings. If the reaction zone can be divided into independent partitions, the treatment of TCI can be greatly simplified. To achieve high-efficiency yet high-fidelity modeling of turbulent reacting flow involving complex chemistry, Dynamic Zone Flamelet Model (DZFM) [40–43] is proposed based on the idea of zonal representational of local TCI. The flamelet zones vary dynamically and adaptively with the flow fields based on the zone division indices, where are defined as pressure, temperature, streamwise distance, and mixture fraction.

DZFM introduces the concept of local conditional variable $Q_\alpha = \langle Y_\alpha|\xi(x,t) = \eta, x \in zone\rangle$, where η means the sampling variable in mixture fraction space, x represents the physical coordinate, $x \in zone$ shows that the coordinate average is confined within the zone. Correspondingly, the instantaneous mass fraction is related to Q_α as

$$Y_\alpha(x,t) = Q_\alpha(\eta = \xi(x,t), x \in zone, t) + Y_\alpha^{'}(x \in zone, t)$$

where $Y_\alpha^{'}$ is the deviation of instantaneous value from the conditional average within the current zone. Note that the $\langle Q_\alpha^{'}|\eta, x \in zone\rangle = 0$ and zone-averaged $\langle Q_\alpha^{'}\rangle_{zone} = \int\langle Q_\alpha^{'}|\eta, x \in zone\rangle P(\eta)d\eta = 0$. $P(\eta)$ represents the probability density function (PDF), which describes the distribution of instantaneous ξ within the zone. For the fact that as the zone shrinks, the fluctuation never disappears but occurs at a low level since the local statistical homogeneity would be valid.

Taking the average on condition that 1) $\xi(x,t) = \eta$ and 2) within the zone $x \in zone$, we can conduct the final governing equation for Q_α as,

$$\rho_\eta \frac{\partial Q_\alpha}{\partial t} + \langle \rho \overrightarrow{U} | \eta \rangle_{zone} \bullet \nabla Q_\alpha + E_{ZFM} = \rho_\eta \frac{D_\alpha}{D_\xi} \langle \chi | \eta \rangle_{zone} \frac{\partial^2 Q_\alpha}{\partial \eta^2} + \rho_\eta \left(\frac{D_\alpha}{D_\xi} - 1 \right) M_\eta \frac{\partial Q_\alpha}{\partial \eta} + \rho_\eta \langle W_\alpha | \eta \rangle \quad (9)$$

with $E_{ZFM} = \frac{\langle \rho \partial Q'_\alpha / \partial t + \rho \vec{U} \cdot \nabla Q'_\alpha - \nabla \cdot (\rho D_\alpha \nabla Q'_\alpha) | \eta \rangle_{zone}}{e_Y} - \langle \rho D \nabla \xi \cdot \nabla (\frac{\partial Q_\alpha}{\partial \eta}) | \eta \rangle_{zone} - \langle \nabla \cdot (\rho D \nabla Q_\alpha) | \eta \rangle_{zone}$

χ is scaler dissipation rate which defined as $\chi = D_\xi (\nabla \xi)^2$, $\rho_\xi = \langle \rho | \eta \rangle$, and the conditional diffusion $M_\eta = \langle \nabla \bullet (\rho D_\xi \nabla \xi | \eta) \rangle_{zone}$. The second term of Eq. (13) shows how the neighbor zones can conduct the convective transport of conditional variables or local flamelets in a flowing manner. So that the downstream can simulate the ignition progress and flame lift-off phenomenon by inheriting the chemical status of upstream. While in the multi-flamelet RIF [39], the ignition process is completed by inheriting the preceding flamelet temperature to a new unburned downstream part. Equation (9) describes the evolution of local flamelet in the region due to convection in the physical space, differential diffusion in the mixture fraction space, and chemical reactions in the species space. The traditional small flame can be regarded as a special area small flame model that treats the entire computational domain as one area. For supersonic cases, the velocity and density can be affected greatly by velocity and mixing fraction. So we can assume that $\langle \overrightarrow{U} | \eta \rangle = \overrightarrow{U}$ and $\langle \rho | \eta \rangle = \rho$, then,

$$\int \langle e_Y | \eta \rangle_{zone} P(\eta) d\eta = \langle e_Y \rangle_{zone} = \frac{\rho \partial \langle Q'_\alpha \rangle_{zone}}{\partial t} + \rho \overrightarrow{U} \bullet \nabla \langle Q'_\alpha \rangle_{zone} - \nabla \bullet \langle \rho D \nabla Q'_\alpha \rangle_{zone} = 0 \quad (10)$$

Using $\eta \in \left[\overline{\xi}_{zone} - \frac{\Delta \xi}{2}, \overline{\xi}_{zone} + \frac{\Delta \xi}{2} \right]$ to define each partition range, where $\overline{\xi}_{zone}$ is the zone averaged mixture fraction and $\Delta \xi$ represents the variation range of the instantaneous mixture fraction within a zone. Through refining the zone division, the scope of $\Delta \xi$ can be controlled to be small enough so that $\langle e_Y | \eta \rangle_{zone} \approx 0$. For the fact that as the zone shrinks, the gradient $\nabla \xi$ never disappears but its variance within the zone occurs at a low level. The final DZFM equation is written as Eq. (4). The conditional scalar dissipation rate $\langle \chi | \eta \rangle$ is modeled by the amplitude mapping closure (AMC) model [44]. The implementation of DZFM can be referred to Yao's work [43].

2.5 Computational Domain and Boundary Conditions

Four sets of unstructured mesh with 7.49 million, 24.67 million, 39.78 million, and 60.04 million are used in this study to verify the grid independence. The axisymmetric main part of the structural grid adopts an O-shaped cell without introducing singularities. The thickness of the first near-wall mesh layer has a thickness of 0.01 mm, and there are a total of 63 layers from the core to the wall. The connection section between the fuel injection and scramjet body introduced a kind of special topology that the two sections can be effectively connected without affecting the O-type grid topology of the main part of the scramjet. In addition, the grid at the fuel hole is further refined. The diameter of the fuel hole is 1.4 mm, the number of grids in the

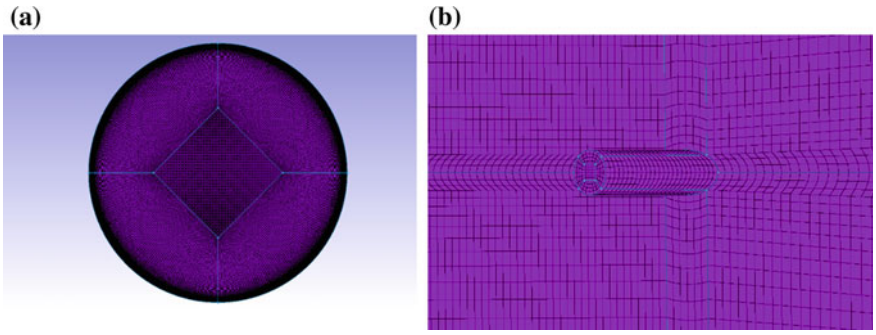

Fig. 2 **a** Mesh clustering around the inlet, **b** mesh clustering around the fuel injectors

circumferential direction of the fuel length is 24, and the maximum grid length is 0.18 mm, which is about 6 times smaller than the average grid size. The body of the fuel hole also used an O-grid topology to guarantee the accuracy of the calculation. The grid length between different parts is adjusted separately to ensure consistency and avoid the adverse effect on the calculation accuracy. Cells distribution on the inlet face and around the fuel injector are shown in Fig. 2.

3 Results and Discussion

3.1 Flow Characteristics

From the pressure contours in Fig. 3, an oblique shock train was formed in the diffuser. The deflection by the diffusor stabilizes the first oblique shock wave. The smooth transition of the diffuser weakens the intensity of the initial shock wave.

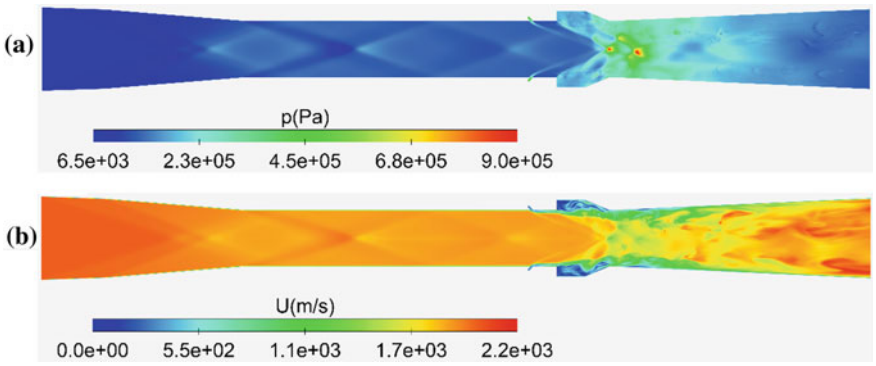

Fig. 3 Contours of **(a)** instantaneous pressure and **(b)** instantaneous velocity

The transverse ethylene injection indices a bow shock wave, which raises both the pressure and temperature to facilitate the subsequent mixing and combustion. The velocity contour shows that an obvious shear layer is generated above the cavity, which develops along the X-direction and is then entrained into the cavity near the aft ramp. The boundary layer in the axisymmetric flow channel is much thinner than rectangular ones due to the absence of the corner effect. The thin boundary layer will lead to a low jet-to-crossflow momentum flux ratio and accordingly low jet penetration depth. For this, axisymmetric scramjets usually have poor mixing and combustion performance.

Figure 4 shows the contours of several key species. From the mass fraction distribution of ethylene, the low jet penetration depth causes insufficient mixing in the jet wake region. Due to the turbulent vortexes developed in the shear/mixing layer above the cavity, noticeable mixing takes place between the ethylene stream and the

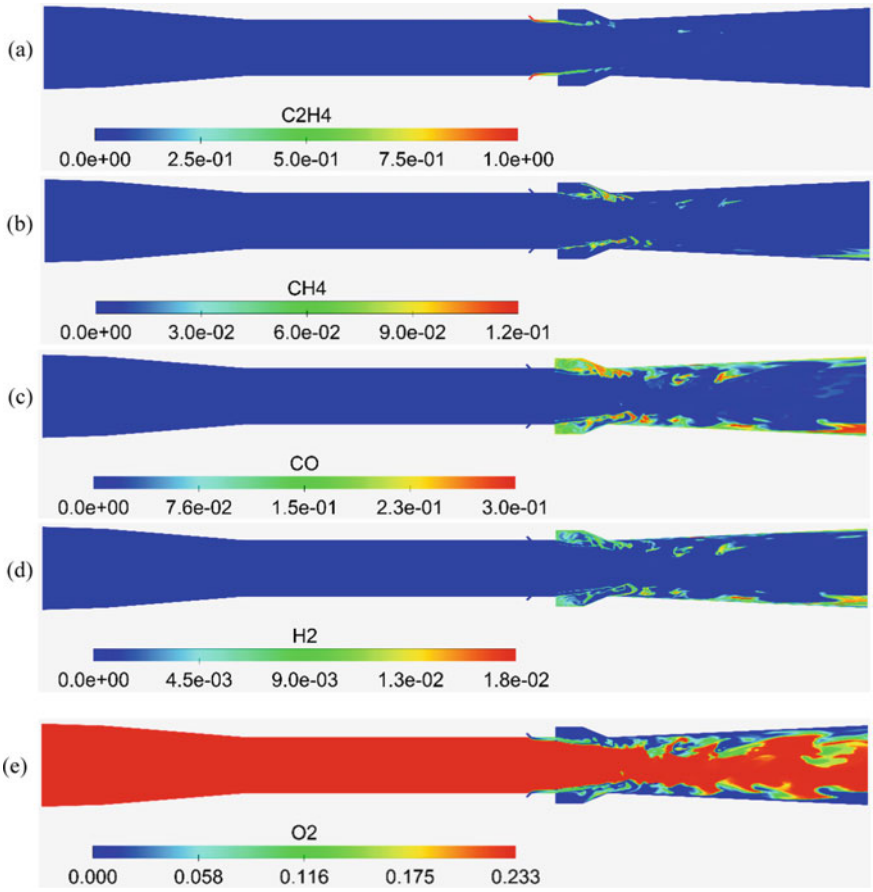

Fig. 4 Contours of instantaneous mass fraction of **a** C_2H_4, **b** CH_4, **c** CO, **d** H_2, **e** O_2

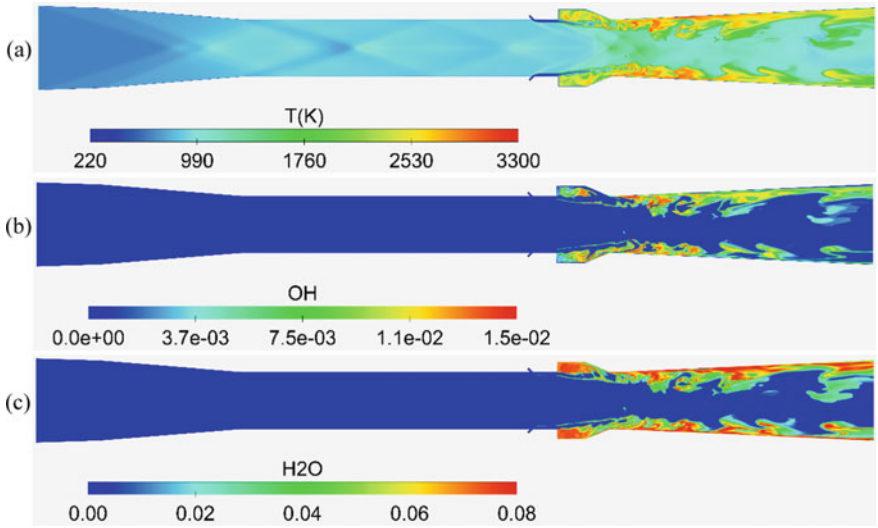

Fig. 5 Contours of **a** temperature, **b** mass fraction of OH, **c** mass fraction of H_2O

main flow. CH_4 is concentrated in the shear layer of the cavity and is entrained into the cavity the recirculation at the rear edge of the cavity, where the main oxidation reactions occur.

A large amount of H_2 and CO concentrate inside the cavity, indicating that the internal recirculation zone premixes the reactants and finally the flame stabilizes in the cavity. Due to the insufficient mixing, there are still some intermediate species that remain at the nozzle exit. These species are asymmetric in their mean distribution, Yao [45] analyzed the influence of symmetry assumption on the supersonic combustion fields and pointed out that minor radical exchange may cause flow asymmetry.

Figure 5 shows the temperature contour. A stable stationary flame zone was formed near the cavity, but the relatively low temperature in the cavity indicates that there is no intense combustion. Intense combustion occurs in the downstream region of the cavity, which is in accordance with the peak of the streamwise pressure distribution. Influenced by the mixing behavior, the combustion exhibits strong pulsations and large coherent structures were formed. As the indicator of the main reaction zone, the distribution of OH is similar to the high-temperature regions with $T > 2000$ K. The low flow speed and high temperature in the recirculation zone provide a favorable bay for the flame holding. For axisymmetric combustors, the absence of corner effect implies a thinner boundary layer that cannot sustain the autoignition of ethylene. Flame holder, like cavity or strut, becomes necessary for the flame stabilization in combustors with a large curvature radius. The H_2O formation indicates that main combustion reactions take place in the cavity and the downstream mixing layer.

3.2 *Role of the Cavity*

Figure 6(a) shows the velocity vector distribution in the cavity. When the incoming flow passes through the front edge, a vortex with a relatively small scale was induced by the sudden expansion in the throughflow area. Under the combined effects of boundary layer displacement and thermal choking, the main flow shrinks towards the center. The crossflow contacts with the aft ramp of the cavity and is entrained into the cavity to form a recirculation zone. Induced by the large recirculation zone, a set of vortexes were formed in the corner of the cavity. These vortex structures can reduce the local velocity and enhance the mixing. Figure 6(b) shows that the subsonic region fills the whole cavity and extends in the reacting layer near the wall. From Fig. 7, the cavity as an ensemble has become a high-temperature region and stable radical pool (e.g. OH), providing a favorable bay for the autoignition and flame stabilization. From Fig. 5, it can be seen that the main combustion reactions start from the cavity. The thermal expansion in the cavity shrinks the throughflow area and enforces the momentum exchange in the above shear/mixing layer, forming large-scale vortexes at the rear edge of the cavity. The subsequent combustion after the cavity thickens the reacting layer attached to the wall and further erodes the supersonic core flow. But till the nozzle exit, the flame did not intersect in the center of the scramjet. There is a narrow low-temperature zone whose temperature is less than 1000 K between the main flow and cavity. It indicates that ethylene did not pyrolyze until it entered the high-temperature region in the cavity.

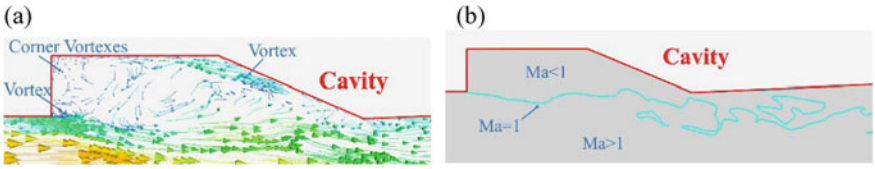

Fig. 6 **a** Velocity vector distribution in the cavity, **b** subsonic region in the cavity

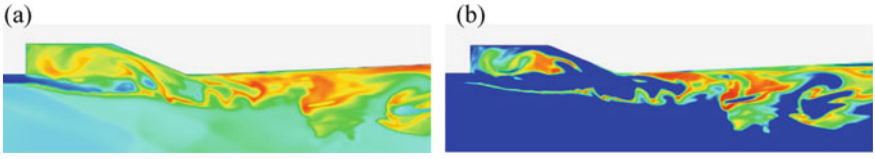

Fig. 7 **a** Temperature distribution in the cavity, **b** OH distribution in the cavity

3.3 Pressure Distribution

Four meshes were used to verify grid independence. The comparison between the simulation results and the experimental results is shown in Fig. 8. The results of the finest mesh are used in the analysis. The current predictions agree well with the experimental data. The agreement in the non-reacting diffuser and isolator sections shows that the solver has a good aerodynamic prediction. The initial abrupt pressure rise is induced by the fuel injection. As it moves downstream, the flame of the combustor induces a major rise in pressure. The modeling results show that the combustor pressure varies smoothly around the cavity, while the experimental data exhibits a large fluctuation in the cavity. The high-temperature gas resides in the cavity all the time, suggesting that there is stable combustion in the cavity, this is consistent with the pressure distribution. The current case has a cavity flame stabilization mode. The transition of combustion mode has a strong dependence on the crossflow conditions, and the investigation of this dynamic process is challenging work. The comparison of combustion model transition between the circular combustor and rectangular combustor has been extensively discussed in Yentsch's work [46]. The experimental results show that the first peak is located in the combustor, farther away from the second peak, and the fluctuation between the two peaks is larger than the modeling results. After the second pressure peak, the measured pressure drops down gradually while the measured pressure has a platform between X = 325 to 370 mm.

As the main feature of DZFM, Fig. 9 shows the evolution of key species in the flamelets probed in the fuel jet wake from the upstream (probe point 1) to the downstream (probe point 7). The primary reaction path in the oxidation of ethylene is $C_2H_4 \rightarrow CH_3 \rightarrow CH \rightarrow CH_2O \rightarrow HCO \rightarrow CO \rightarrow CO_2$ [47]. As the first species that is pyrolyzed from the original fuel C_2H_4, CH3 is richer in the fuel jet wake and gradually consumed as the reaction proceeds. CH radical is then formed through the H-abstraction reaction of CH_3/CH_2, but will be quickly consumed by H_2O or O_2 to produce into CH_2O and HCO. The formation of formaldehyde (CH_2O) usually indicates the success of ignition. Produced in a chain-carrying step and with high activity, the existence of CH_2O is usually short, and after the ignition point,

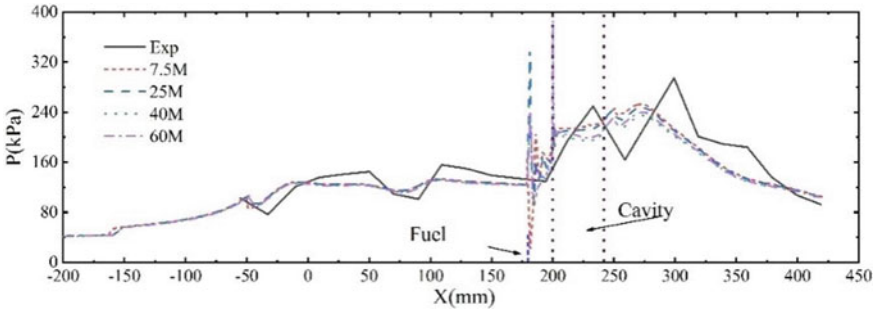

Fig. 8 Mean wall pressure in the streamwise direction

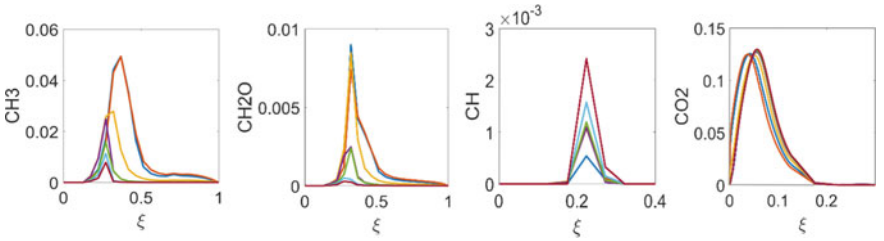

Fig. 9 Evolution of flamelet variables along the flow path

it is quickly converted into more active formyl radical (HCO) and H_2. HCO can be consumed by any oxygenated species (CO, O_2), H, and third-party species to produce CO. The further conversion of CO to the final stable product CO_2 usually occurs in the post-ignition region. The concentration of CO_2 increases as the reaction towards equilibrium and the well-known rich-shifting phenomenon [48] is observed.

4 Conclusions

This study conducts a Large Eddy Simulation of an axisymmetric scramjet based on DZFM. The predicted pressure agrees well with the experimental data. The grid convergence was verified by using four mesh sets, with 7.5 million, 25 million, 40 million, and 60 million cells respectively. Due to the absence of the corner effect, the boundary layer is thinner and the jet penetration depth is much lower. The poor mixing between the transverse fuel jet and the crossflow causes weak combustion and a low-pressure rise ratio of around 3. The cavity plays a key role in stabilizing the flame by increasing the flow residence time, enhancing mixing, and preheating the reactants. Axisymmetric scramjets overall have poor mixing and combustion performance, unless used together with efficient flame holders. Researchers should focus more on the variations of the axisymmetric combustor, e.g. elliptic scramjets, or rectangular scramjets with rounding corners.

Acknowledgements This article is funded by National Key Research and Development Program of China (2019YFB1704200)

References

1. Weber RJ, Mackay JS (1958) An analysis of ramjet engines using supersonic combustion. Lewis Flight Propulsion Laboratory, Washington, DC
2. Billig FS (1993) Research on supersonic combustion. J Propul Power 9(4):499–514. https://doi.org/10.2514/3.23652

3. Mehta UB (1996) Strategy for developing air-breathing aerospace planes. J Aircr 33(2):377–385. https://doi.org/10.2514/3.46948
4. Curran ET (2001) Scramjet engines: The first forty years. J Propul Power 17(6):1138–1148. https://doi.org/10.2514/2.5875
5. Seleznev RK, Surzhikov ST, Shang JS (2019) A review of the scramjet experimental data base. Prog Aerosp Sci 106:43–70. https://doi.org/10.1016/j.paerosci.2019.02.001
6. Liu Q, Baccarella D, Lee T (2020). Review of combustion stabilization for hypersonic airbreathing propulsion. Prog Aerosp Sci 119. https://doi.org/10.1016/j.paerosci.2020.100636
7. Das N, Pandey KM, Sharma KK (2021). A brief review on the recent advancement in the field of jet engine scramjet engine. Materials today: Proceedings. https://doi.org/10.1016/j.matpr.2020.12.1035
8. Yu G, Li JG, Chang XY et al (2001) Investigation of kerosene combustion characteristics with pilot hydrogen in model supersonic combustors. J Propul Power 17(6):1263–1272. https://doi.org/10.2514/2.5874
9. Heiser WH, Pratt DT (1994) Hypersonic airbreathing propulsion. AIAA, Washington
10. Sydenham (2006) The rebirth of round hypersonic propulsion. 42nd AIAA/ASME/SAE/ASEE joint propulsion conference & exhibit. https://doi.org/10.2514/6.2006-5035
11. Vanyai T, Grieve S, Street O et al (2019) Fundamental scramjet combustion experiments using hydrocarbon fuel. J Propul Power 35(5):953–963. https://doi.org/10.2514/6.2018-5201
12. Liu Q, Baccarella D, Lee T et al (2017) Influences of inlet geometry modification on scramjet flow and combustion dynamics. J Propul Power 33(5):1179–1186. https://doi.org/10.2514/1.B36434
13. Denman ZJ, Chan WYK, Brieschenk S et al (2016) Ignition experiments of hydrocarbons in a Mach 8 shape-transitioning scramjet engine. J Propul Power 32(6):1462–1471. https://doi.org/10.2514/1.B36099
14. Barnes FW, Segal C (2015) Cavity-based flameholding for chemically-reacting supersonic flows. Prog Aerosp Sci 76:24–41. https://doi.org/10.1016/j.paerosci.2015.04.002
15. Weller HG, Tabor G, Jasak H et al (1998) A tensorial approach to computational continuum mechanics using object-oriented techniques. Comput Phys 12(6). https://doi.org/10.1063/1.168744
16. Kee RJ, Rupley FM, Miller JA (1989) Chemkin-Ii: A Fortran chemical kinetics package for the analysis of gas-phase chemical kinetics. Sandia National Laboratories, Albuquerque, TR SAND89-8009B
17. Kurganov A, Tadmor E (2000) New high-resolution central schemes for nonlinear conservation laws and convection-diffusion equations. J Comput Phys 160(1):241–282. https://doi.org/10.1006/jcph.2000.6459
18. Greenshields CJ, Weller HG, Gasparini L et al (2009) Implementation of semi-discrete, non-staggered central schemes in a collocated, polyhedral, finite volume framework, for high-speed viscous flows. Int J Numer Meth Fluids 38(2):139–161. https://doi.org/10.1002/fld.2069
19. Vuorinen V, Larmi M, Schlatter P et al (2012) A low-dissipative, scale-selective discretization scheme for the Navier-Stokes equations. Comput Fluids 70:195–205. https://doi.org/10.1016/j.compfluid.2012.09.022
20. Chase MW (1998) NIST-JANAF thermochemical tables 2 volume-set (journal of physical and chemical reference data monograph 9). monograph 9. American Institute of Physics, Maryland, pp 1–1952. https://doi.org/10.1063/1.555993
21. Greenshields CJ, Weller HG, Gasparini L et al (2009) Implementation of semi-discrete, non-staggered central schemes in a colocated, polyhedral, finite volume framework, for high-speed viscous flows. Int J Numer Meth Fluids 63:1–21. https://doi.org/10.1002/fld.2069
22. Wu K, Li X, Yao W et al (2015). Three-dimensional numerical study of the acoustic properties of a highly under expanded jet. 20th AIAA international space planes and hypersonic systems and technologies conference. https://doi.org/10.2514/6.2015-3572
23. Li X, Wu K, Yao W et al (2015) A Comparative Study of Highly Underexpanded Nitrogen and Hydrogen Jets Using Large Eddy Simulation.20th AIAA international space planes and hypersonic systems and technologies conference. https://doi.org/10.1016/j.ijhydene.2016.01.120.

24. Li X, Yao W, Fan X (2016) Large-eddy simulation of time evolution and instability of highly under expanded sonic jets. AIAA J 54(10):3191–3211. https://doi.org/10.2514/1.J054689
25. Li X, Zhou R, Yao W et al (2017) Flow characteristic of highly under expanded jets from various nozzle geometries. Appl Therm Eng 125:240–253. https://doi.org/10.1016/j.applthermaleng.2017.07.002
26. Li X, Fan E, Yao W et al (2017) Numerical investigation of characteristic frequency excited highly under expanded jets. Aerosp Sci Technol 63:304–316. https://doi.org/10.1016/j.ast.2017.01.005
27. Yachao L, Yao W, Fan X (2017). A low-dissipation scheme based on OpenFoam designed for large eddy simulation in compressible flow.21st AIAA international space planes and hypersonics technologies conference. https://doi.org/10.2514/6.2017-2444.
28. Yao W, Wang J, Lu Y et al (2015) Full-scale detached eddy simulation of kerosene fueled scramjet combustor based on skeletal mechanism. 20th AIAA international space planes and hypersonic systems and technologies conference. https://doi.org/10.2514/6.2015-3579.
29. Wu K, Zhang P, Yao W et al (2017) Numerical investigation on flame stabilization in DLR hydrogen supersonic combustor with strut injection. Combust Sci Technol 189(12):2154–2179. https://doi.org/10.1080/00102202.2017.1365847
30. Yao W, Lu Y, Li X et al (2016) Improved delayed detached eddy simulation of a high-ma active-cooled scramjet combustor based on skeletal kerosene mechanism. 52nd AIAA/SAE/ASEE joint propulsion conference. https://doi.org/10.2514/6.2016-4761
31. Yao W, Yuan Y, Li X et al (2018) Comparative study of elliptic and round scramjet combustors fueled by RP-3. J Propul Power 34(3):772–786. https://doi.org/10.2514/1.B36721
32. Wu K, Yao W, Fan X (2017) Development and fidelity evaluation of a skeletal ethylene mechanism under scramjet-relevant conditions. Energy Fuels 31(12):14296–14305. https://doi.org/10.1021/acs.energyfuels.7b03033
33. Yao W, Lu Y, Wu K et al (2018) Modeling analysis of an actively cooled scramjet combustor under different kerosene/air ratios. J Propul Power 34(4):975–991. https://doi.org/10.2514/1.B36866
34. Fureby C, Moller SI (1995) Large eddy simulation of reacting flows applied to bluff body stabilized flames. AIAA J 33(12):2339–2347. https://doi.org/10.2514/3.12989
35. Candler GV, Martín MP, Piomelli U (2000) Subgrid-scale models for compressible large-eddy simulations. theoretical & computational fluid dynamics. Theoret Comput Fluid Dyn. https://doi.org/10.1007/PL00020896
36. Tramecourt N, Menon S, Amaya J (2004). LES of Supercritical Combustion in a Gas Turbine Engine. 40th AIAA/ASME/SAE/ASEE joint propulsion conference and exhibit. https://doi.org/10.2514/6.2004-3381
37. Kundu P, Pei Y, Wang M et al (2014) Evaluation of turbulence-chemistry interaction under diesel engine conditions with multi-flamelet RIF model. Atom Sprays 24(9):779–800. https://doi.org/10.1615/AtomizSpr.2014010506
38. Shur ML, Spalart PR, Strelets MK, Travin AK (2008) A hybrid RANS-LES approach with delayed-des and wall-modelled LES capabilities. Int J Heat Fluid Flow 29:1638–1649. https://doi.org/10.1016/j.ijheatfluidflow.2008.07.0
39. Spalart PR, Allmaras SR (1992) A one-equation turbulence model for aerodynamic flows. AIAA-92-0439, January 6–9. https://doi.org/10.2514/6.1992-439
40. Yao W, Fan X (2017) Development of zone flamelet model for scramjet combustor modeling. 21st AIAA international space planes and hypersonic systems and technology conference. http://dspace.imech.ac.cn/handle/311007/72183
41. Yao W, Li B (2019) Application of dynamic zone flamelet model to a GH2/GO2 rocket combustor. AIAA Propulsion and Energy 2019 Forum. https://doi.org/10.2514/6.2019-3868
42. Yao W, Liu H, Xue L et al (2021) Performance analysis of a strut-aided hypersonic scramjet by full-scale IDDES modeling. Aero Sci Tech 117:106941. https://doi.org/10.1016/j.ast.2021.106941
43. Yao W (2020) On the application of dynamic zone flamelet model to large eddy simulation of supersonic hydrogen flame. Int J Hydrogen Energy 45(41):21940–21955. https://doi.org/10.1016/j.ijhydene.2020.05.189

44. O'brien EE, Jiang TL (1991) The conditional dissipation rate of an initially binary scalar in homogeneous turbulence. Phys Fluids A Fluid Dyn 3(12):3121–3123. https://doi.org/10.1063/1.858127
45. Yao W, Wu K, Fan X (2019) Influences of domain symmetry on supersonic combustion modeling. J Propul Power 35(2):451–465. https://doi.org/10.2514/1.B37227
46. Yentsch RJ, Gaitonde DV (2014) Comparison of mode-transition phenomena in axisymmetric and rectangular scramjet flowpaths. 52nd Aerospace Sciences Meeting. https://doi.org/10.2514/6.2014-0625
47. Warnatz J (1981) The structure of laminar alkane-, alkene-, and acethylene flames. Eighteenth Symp Combus 18:369–384. https://doi.org/10.1016/S0082-0784(81)80042-2
48. Law CK, Makino A, Lu TF (2006) On the Off-stoichiometric peaking of adiabatic flame temperature. Combust Flame 145:808–819. https://doi.org/10.1016/j.combustflame.2006.01.009